Batteries & Supercaps

Research Article
doi.org/10.1002/batt.202400176

Chemistry
Europe
European Chemical
Societies Publishing

www.batteries-supercaps.org

A Flexible One-Dimensional Woven Supercapacitor for Low-Power Smart Electronic Textiles

Abhinav Tandon,[b] Shalu Rani,[b] and Yogesh Sharma*[a]

Flexible energy storage devices are attracting a great attention nowadays in the rapidly growing area of implantable/wearable electronics. This bloom has generated great demands on flexible wire-shaped supercapacitors (WSC) as power sources in wearable electronic systems that can offer tunable sizes, shapes, and versatile designs. Herein, a flexible WSC is fabricated using $MgMn_2O_4$ nanofibers (MMO-NFs) over a flexible carbon yarn substrate via the electrophoretic deposition method in the first report. The binder-free deposition of highly porous and one-dimensionally aligned MMO-NFs over carbon yarn offers excellent ionic/charge transport into the fabricated device. The assembled WSC device at 0.1 mA/cm current rate shows capacitances of 386 mF/cm^2 and 45.5 mF/cm. A capacitance retention of 88% for a WSC device after 10,000 cycles indicates its good cyclability. Further, the WSC exhibits good flexibility, retaining 94% of capacitance at 0.5 mA/cm after 2000 bending cycles. Furthermore, the flexible WSC device shows power and energy density of 744 μW/cm and 14.2 μWh/cm, respectively. Additionally, WSC devices demonstrate their practical energy storage capabilities in a video that shows three similar devices being knitted into a wearable glove and glowing a red light-emitting diode (LED) for more than five minutes in various bending positions.

1. Introduction

During the past few decades, the emerging electronic device industry requires wearability, multifunctionality, safety, miniaturized tunable-shaped components and the integration of these components into the cloths or garments/textiles.[1–4] Recently, various wearable fiber-based batteries have been utilized as energy storage devices inside these wearable textiles.[2,5,6] However, the fabrication of yarn-shaped batteries is quite complex because of the involvement of complex fabrication setups, flammability, and leakage issues of the electrolytes used for batteries.[7] Utilizing supercapacitors (SCs) as energy storage components in wearable electronics offers several advantages over batteries, including ease of fabrication at room temperature, higher power density, and better cyclic stability.[8] However, conventional SCs suffer from several drawbacks such as incompatibility, larger size and heavy weight, and lack of flexibility and strength for flexible wearable electronic applications.[9] Therefore, as an innovative energy storage device, flexible wire-shaped SC (WSC) has the potential to be integrated/knitted into the wearable fabric without losing its original architecture, flexibility, and mechanical stability for its application in integrated multifunctional electronic systems, such as energy harvesters and sensors.[1,10] The wire-shaped current collector is the backbone of the WSC device that can offer lightweight, mechanical flexibility, strength, and wearability to the device. Generally, the current collectors of metal wires like Pt, Au, and stainless steel (SS) are used in WSCs.[1,11,12] The main drawbacks of metal wire current collectors are their heavier weight, less flexibility, difficulty weaving in wearable textiles, and deteriorating the wearing comfortability of the smart textile without any capacitive energy storage contribution.[13] Further, various CNT yarn-based flexible SCs have been developed for wearable electronics applications, where CNT yarns provide flexibility and electrical conductivity.[14,15] However, the primary limitations of CNT yarns include their high cost, limited mechanical strength under certain conditions, and difficulties in attaining uniformity and scalability in production. Therefore, one of the cost-effective alternatives for metal current collectors and CNT yarns is low-density carbon yarns that can offer high mechanical flexibility and electrical conductivity to the WSC device.[16,17]

The electrochemical performance of WSC devices mainly depends upon their active electrode materials. Recently, manganese (Mn)-based oxides, specifically spinel $MgMn_2O_4$ nanofibers (MMO-NFs), have attracted more attention as a promising active electrode material for the SCs because of their one-dimensionally aligned porous nature, high aspect ratio, high specific surface area, cost-effectiveness, abundance, and environmental-friendly nature. These properties can effectively enhance the percolation and transportation of electrolytic ions, thereby reducing the ohmic/charge-transfer resistance and improving the electrochemical performance.[18] Further, the development and utilization of $MgMn_2O_4$ nanofibers with oxygen defects/vacancies can enhance the system's electrical conductivity and rate capability. A higher concentration of oxygen vacancies facilitates more efficient electronic and ionic

[a] Y. Sharma
Department of Physics and Joint Faculty, Center for Sustainable Energy
Indian Institute of Technology Roorkee
Roorkee, 247667, Uttarakhand, India
E-mail: yogesh.sharma@ph.iitr.ac.in

[b] A. Tandon, S. Rani
Department of Physics
Indian Institute of Technology Roorkee
Roorkee, 247667, Uttarakhand, India

🖵 Supporting information for this article is available on the WWW under
https://doi.org/10.1002/batt.202400176

Batteries & Supercaps

Research Article
doi.org/10.1002/batt.202400176

Chemistry Europe
European Chemical
Societies Publishing

mobility, resulting in improved charge kinetics, even at elevated rates.

Conventional supercapacitors (SCs) are often rigid, inflexible, and bulky, comprising active materials coated with binders on current collectors within their electrodes. However, these binders, being electrochemically inactive, add dead weight to the electrode. In contrast, the facile electrophoretic deposition (EPD) technique is employed, depositing the active material onto the current collector without incorporating any binding agent. Moreover, the EPD technique offers the advantages of room temperature deposition, precise control over process parameters, and cost-effectiveness, making it a safer and more economical option.[13] Therefore, in this work, a flexible all-solid-state WSC device is fabricated by employing in situ co-electrophoretic deposition of MMO-NFs and MWCNT (used as an electronic conductive additive) over low-density flexible carbon yarn in the first report for application in flexible wearable electronics. The fabricated WSC device shows excellent electrochemical performance, flexibility and mechanical stability. In order to demonstrate its practical applicability, three identical WSC devices are knitted within a wearable hand glove and glowing a red LED for more than five minutes in various bending positions, demonstrating the versatility of the WSC device in flexible wearable multifunctional electronic applications.

Experimental Section

Fabrication of MMO Nanofibers

The detailed fabrication process of the active material electrodes and devices is presented in Figure 1. First, a facile electrospinning technique is used to fabricate MMO-NFs. In order to fabricate MMO-NFs, 2 mmol of manganese acetate tetrahydrate and 1 mmol of magnesium acetate tetrahydrate are mixed in DI water (1 ml) and stirred continuously till the solution becomes clear. In parallel, a solution of PVP (10 wt%) is prepared in ethanol (8.1 ml) and stirred at room temperature for 1 h. Then, the prepared solutions are continuously mixed together for 10 hours to achieve a transparent and clear solution. In the following steps, the final solution will be loaded into a syringe (5 ml) and ejected through a stainless steel (SS) spinneret using high-voltage (16 kV) DC power supplies. An aluminium (Al) foil is wrapped around the drum collector and fixed at a distance of approximately 11 cm from the spinneret. At a fixed flow rate of 1 ml/h, the solution mixture is ejected through the nozzle. The humidity $18(\pm 3)\%$ and relative temperature ($38\,°C$) inside the electrospinning chamber are fixed. Further, the collected as-spun MMO/PVP nanofiber sheets are dried overnight at $80\,°C$ under a vacuum, followed by calcination at several temperatures in air. The pure phase and most oxygen deficient form of MMO-NFs without any impurities was successfully obtained by calcinating as-spun NFs at $600\,°C$ temperature for 4 hours with a heating rate of $1\,°C\,min^{-1}$.

Fabrication of the Electrodes via EPD

As purchased multiwalled carbon nanotubes (MWCNTs) was purified via the reflux process. For the electrode fabrication via EPD, MMO-NFs are added to the ethanol and ultrasonicated for 30 min to prepare a dispersed solution. In addition to MMO-NFs, MWCNTs (2 wt%) are also added to the dispersion in order to increase the coated electrode conductivity and MMO-NFs adhesion as illustrated in Figure 1a. In electrophoresis, the dispersion with the electrically charged surface of the active materials is required so that they can move towards oppositely charged electrodes on the application of the electric field. Prior to ultrasonication for the cathodic EPD process, a 100 μl of 36.4 wt% HCl as a charging agent is mixed with the prepared solution to create a positive electrical charge on the surface of the active material. Zeta potential, the charge on a dispersed particle within a solution, is identified by a ZS90 Malvern Zetasizer Nano software and found to be 36 mV. Prior to the deposition process, bare carbon yarns undergo a sequence involving washing with deionized water and acetone. Subsequently, they are subjected to heat treatment at $450\,°C$ for 2 h to
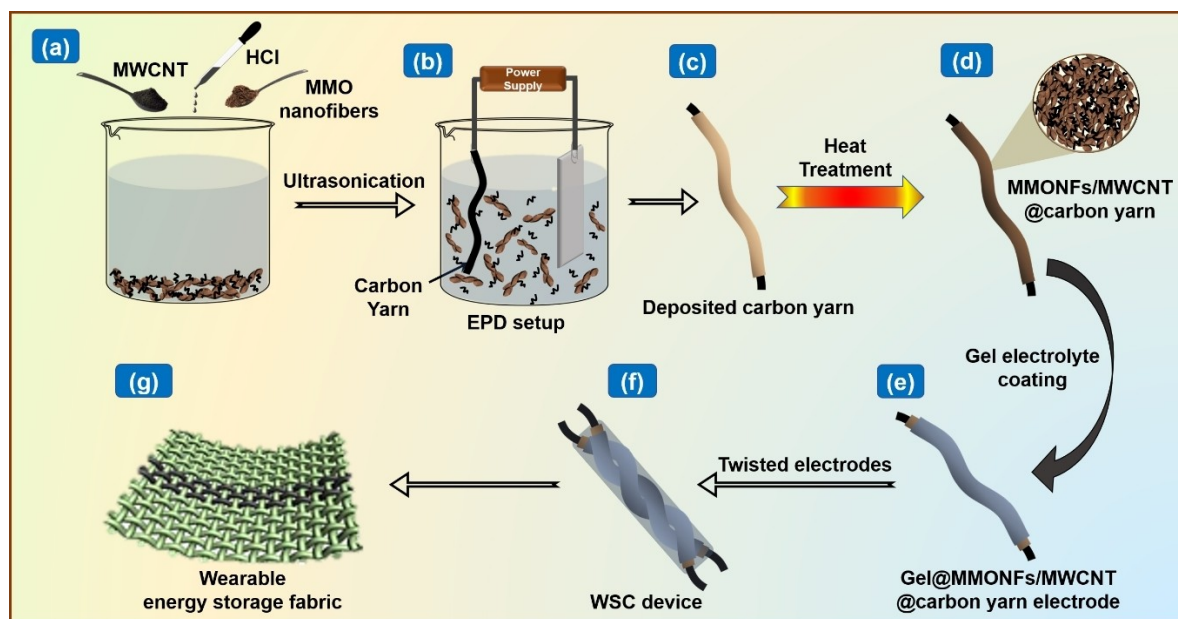

Figure 1. Schematic of fabrication process flow for flexible WSC device.

Batteries & Supercaps

Research Article
doi.org/10.1002/batt.202400176

Chemistry Europe
European Chemical
Societies Publishing

activate their surface. To investigate the effect of heat treatment on carbon yarn's strength, we conducted a tensile strength analysis of carbon yarn before and after heat treatment, as shown in Supporting Information (Figure S1). The tensile stress-strain curve of the carbon yarn is measured using a universal testing machine. Both the samples, before and after heat treatment, show a good tensile performance with fracture stress of 65.7 and 58.7 MPa with the break elongation of 8.82% and 8.43%, respectively. It is worth noting that there isn't a significant difference in the strength of the carbon yarn before and after the heat treatment. The tensile properties of both samples are comparable to the reported literature,[19–21] hence indicating the good stress-bearing capability of the carbon yarn. In the EPD setup (Figure 1b), activated carbon yarn and SS plate are used as cathode and anode, respectively. Within the dispersed solution of active materials, the cathode and anode are submerged, maintaining a separation distance of 1 cm between them and a 45 V constant DC voltage is applied for a deposition time of 10 minutes. Then, the MMO-NFs/MWCNT deposited carbon yarn electrodes (Figure 1c and d) are dried in a vacuum for 12 h at 60°C. The length of the single MMO-NFs/MWCNT deposited carbon yarn electrode is 10 cm. The active materials loading onto the carbon yarn is 0.25 mg/cm. In this process, MMO nanofibers and MWCNT are co-deposited by EPD technique, leading to a hierarchical modified architecture of the composite yarn electrode.

All-Solid-State WSC Device Fabrication

To fabricate the WSC device, a gel electrolyte (PVA-H_3PO_4-Na_2MoO_4) is prepared. First, 6 g of polyvinyl alcohol (PVA) is dissolved into 60 ml of DI water via constant stirring at 90°C temperature till a transparent solution is obtained.[22] Then, 1 M H_3PO_4 is mixed to the PVA solution via stirring for 30 min. Further, a small quantity of sodium molybdate (Na_2MoO_4) solution (40 mM) is introduced into the prepared mixture, and the resulting solution is continuously agitated for another half hour. All-solid-state flexible WSC devices are constructed by soaking MMO-NFs/MWCNT coated yarn electrodes in a prepared electrolyte for an hour and dried at room temperature for 10–12 hours, as illustrated in Figure 1e. Then, 2 equal gel-coated yarns are twisted together and coated again with gel electrolyte and dried for 10–12 hours at room temperature, as presented in Figure 1f. During this process, multilayering of gel electrolyte may be done carefully to keep the thickness of electrolyte coating uniform. However, since it's a manual process, slight variations in thickness and fiber circumference may be anticipated, though they are controllable. Here, gel serves as both the electrolyte and separator between two electrodes coated with MMO-NFs/MWCNT. The WSC device has a total remaining length of 6 cm after twisting the electrodes. Further, the as-fabricated electrodes and devices are characterized. The WSC device based on MMO-NFs/MWCNT@carbon yarn is named as MC-WSC. Figure 1g shows the illustration of a knitted WSC device in a wearable fabric. For comparison, two WSC devices have also been fabricated based on MMO-NFs@carbon yarn (without MWCNT) and bare carbon yarn (without a coating of active materials) named as M-WSC and C-WSC, respectively.

Characterization

The microstructure of as-fabricated MMO-NFs and electrodes is investigated using a field-emission scanning electron microscope (FESEM, Carl-Zeiss Gemini). The energy-dispersive X-ray spectroscopy (EDX, Carl Zeiss) is used to measure the mapping and elemental composition of the MMO-NFs & electrodes. Thermogravimetric analyzer (TG, SII 6300 EXSTAR) is employed to determine the

decomposition of the as-spun nanofibers with temperature under an air atmosphere. The crystallinity of the MMO-NFs is examined using a Rigaku X-ray diffractometer (XRD, CuK_α). Subsequently, the XRD data underwent Rietveld refinement via the PDXL2 software. To assess the surface area and pore size distribution (PSD), the MMO-NFs were analyzed at 77 K using ASIQWIN BET surface area analyzer (Quantachrome). X-ray photoelectron spectroscopy (XPS, PHI 5000 Versa Probe III) is used to investigate the chemical composition and elemental state of MMO-NFs. The fabricated WSC devices are electrochemically characterized in a two-electrode setup via cyclic voltammogram (CV) and galvanostatic charge/discharge (GCD) utilizing an AUTOLAB Potentiostat/Galvanostat (MAC-80,039) instrument. The current rates of 0.1–1 mA/cm and the scan rates of 10–100 mV/s are applied in GCD and CV, respectively, in a 0–1.5 V voltage window. Electrochemical impedance spectroscopy (EIS) is utilized to measure the impedance data plots of MMO-NFs and as-fabricated WSCs by applying a voltage of 5 mV and frequency of 100 kHz-0.01 Hz. For the WSC device, the values of linear capacitance (C_L), areal capacitance (C_A), and volumetric capacitance (C_V) are calculated by equations 1, 2, and 3, respectively. The areal capacitance from CV is calculated using equation 4. The linear energy density (E_L), linear power density (P_L), and areal energy density (E_A) are determined using equations 5, 6, and 7, respectively.[21,23]

$$C_L \text{ (F/cm)} = \frac{I\Delta t}{V} \tag{1}$$

$$C_A \text{ (F/cm}^2) = \frac{4C}{A_{Device}} \tag{2}$$

$$C_V \text{ (F/cm}^3) = \frac{4C}{V_{Device}} \tag{3}$$

$$C_A \text{ (F/cm}^2) = \frac{\int_{-V}^{V} i \, dV}{V. \, \nu. \, A_{Device}} \tag{4}$$

$$E_L \text{ (Wh/cm)} = \frac{1}{2 \times 3600} C_L V^2 \tag{5}$$

$$P_L \text{ (W/cm)} = \frac{E_L}{\Delta t} \times 3600 \tag{6}$$

$$E_A \text{ (Wh/cm}^2) = \frac{1}{2 \times 3600} C_A V^2 \tag{7}$$

where Δt represents the discharge time (s), V is the applied voltage window (V), ν is the scan rate (V/s), i is the current (mA), I is the current rate for discharge (mA/cm), and $C = (\Delta t \times i)/V$.[24,25] The volume (cm^3) and surface area (cm^2) of the device are measured using $V_{Device} = L\pi(D/2)^2$ and $A_{Device} = L\pi D$, respectively, where D denotes the WSC device diameter containing both electrodes (cm), and L indicates its length (cm).

2. Results and Discussion

The morphological characteristics of the fabricated MMO-NFs were examined using FESEM. The nanofibers in their as-spun state exhibited a uniform and smooth surface texture, with a diameter of approximately 430 ($\pm$30) nm, as shown in Figure 2a. Thermal analysis was conducted on freshly spun nano-

Batteries & Supercaps

Research Article
doi.org/10.1002/batt.202400176

Chemistry Europe
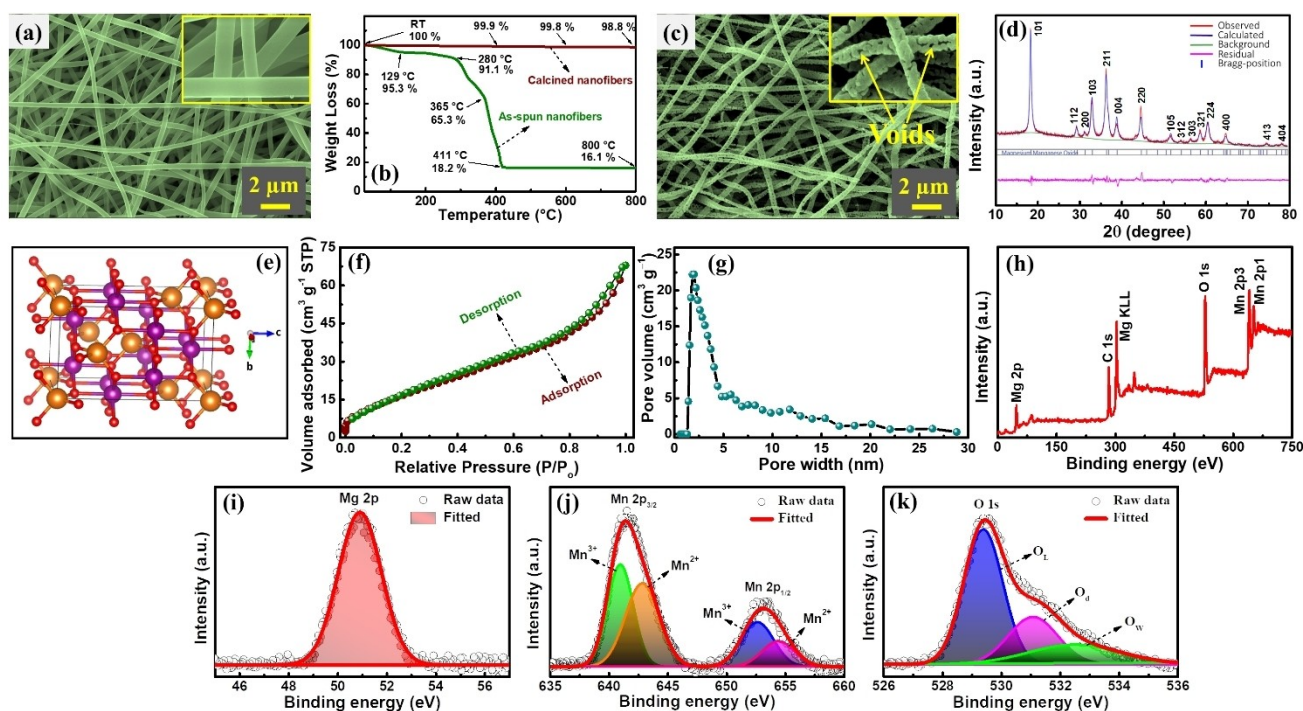European Chemical
Societies Publishing

Figure 2. Surface morphology of (a) as-spun and (b) calcined MMO-NFs, (c) XRD spectra and (d) XPS survey spectra of MMO-NFs, and high-resolution XPS spectra of (e) Mg 2p, (f) Mn 2p, and (g) O 1s. (h) Multipoint BET isotherm.

fibers using TGA, spanning temperatures from room temperature (RT) to 800 °C, as depicted in Figure 2b. Initially, a weight loss of 8.9% occurred between RT and 280 °C, ascribed to the removal of residual solvents like ethanol and absorbed moisture. Subsequently, a pronounced decline in weight percentage occurred within 365–400 °C, indicating the elimination of the MMO-NFs polymeric backbone.[18] Moreover, the weight loss observed between 400 and 800 °C was negligible, suggesting that the constant weight illustrates the residual removal from the nanofibers. Upon calcination at 600 °C, the MMO-NFs (as depicted in Figure 2c) maintained their uniform and one-dimensional morphology, featuring gaps or voids between individual nanoparticles within the nanofibers. The presence of optimal morphological gaps or voids within the nanofibers performs as reactive sites for external ions, thus bolstering charge storage properties.[18,26] It's noteworthy that MMO benefits from a slower heating rate of 1 °C/min to achieve a porous nanofibrous structure with an increased surface area. This slower rate facilitates the nucleation and growth of MMO nanoparticles and allows for the gradual decomposition of PVP, creating a favorable environment. Moreover, to assess the elemental distribution within the MMO-NFs, we analyzed the EDX spectra. The EDX spectrum, as depicted in Supporting Information (Figure S2a), demonstrates that the atomic ratio of Mg, Mn, and O is well-balanced and aligns with the stoichiometry of the precursors employed in MMO-NF fabrication and aligns with the stoichiometry of the precursors employed in MMO-NF fabrication. Further, the EDX elemental mapping, as depicted in Figure S2b, verifies the even spreading of O, Mg, and Mn elements on the surface of MMO-NFs.

The crystal structure of the calcined MMO-NFs was identified using the XRD technique. The XRD patterns of MMO-NFs after Rietveld refinement are illustrated in Figure 2d, with the respective refinement parameters detailed in Table 1. The XRD pattern shows the corresponding diffraction peaks of the tetragonal MMO structure in accordance with the JCPDS card no.: 04-006-8110 with $I4_1/amd$ space group.[27] Moreover, the crystallographic configuration of MMO-NFs, derived from the refined data, is depicted in Figure 2e. In this representation, red, grey, and green spheres symbolize O, Mn, and Mg atoms, respectively, with Mg occupying the tetrahedral and Mn occupying the octahedral positions. By applying Scherrer's equation ($t = 0.9\lambda/\beta\cos\theta$), the average crystallite size of the MMO-NFs was found to be 14($\pm$2) nm, where λ represents the X-ray wavelength (1.54 Å), β is a full-width half maximum of the (101) plane, θ is the Bragg's angle of diffraction, and t is the mean crystallite size.

Figure 2f displays the nitrogen adsorption-desorption isotherm plot of MMO-NFs, which exhibits a characteristic isotherm of type-IV within the pressure range (P/P$_0$) of 0 to 1.0. The

Table 1. Crystallographic parameters for MMO-NFs after refinement: $a = b = 5.732$ (9) Å, $c = 9.256$ (3) Å, R_{exp} (%): 4.25, R_{wp} (%): 6.26, R_p (%): 4.63, S: 1.47, and χ^2: 2.16.

Elements	x	y	z	Occupancy
O	0.000000	0.5144(8)	0.2392(4)	1.000
Mg	0.000000	0.250000	0.375000	1.000
Mn	0.000000	0.000000	0.000000	1.000

Batteries & Supercaps

Research Article
doi.org/10.1002/batt.202400176

**Chemistry
Europe**
European Chemical
Societies Publishing

MMO-NFs exhibit a specific surface area of $71 (\pm 2)$ m^{2}g^{-1}. Furthermore, pore size distributions were determined using the DFT method, as shown in Figure 2g. Notably, most pores are concentrated around $3 (\pm 1)$ nm, with $0.094 (\pm 0.002)$ cc g^{-1} pore volume. The presence of a microporosity and high surface area within the MMO-NFs could offer extra active sites for foreign ions, potentially enhancing the electrochemical performance at the electrode-electrolyte interface.[28]

In order to determine the chemical composition of the as-fabricated MMO-NFs, XPS was performed. In Figure 2h, the survey spectra demonstrate the presence of Mn, Mg, and O elements in MMO-NFs. The high-resolution spectra of Mg 2p, as shown in Figure 2i, indicate the presence of Mg^{2+} at 50.92 eV.[29] Further, the Mn 2p spectra (Figure 2j) for the MMO-NFs reveal two spin-orbit doublets of Mn 2p$_{1/2}$ and Mn 2p$_{3/2}$ at 653.33 and 641.77 eV, respectively, exhibiting 11.56 eV spin-orbit splitting. The Mn 2p$_{1/2}$ and Mn 2p$_{3/2}$ fitted spectra show peaks corresponding to Mn^{2+} (642.5, 654.1 eV) and Mn^{3+} (641.2, 652.6 eV) states, respectively. In the MMO-NFs, the presence of Mn^{2+} indicates the existence of oxygen defects. This observation aligns with previous findings in oxygen-deficient materials.[30] Furthermore, Figure 2k presents high-resolution O 1s spectra, revealing the presence of three distinct peaks. These peaks are observed at binding energies of 532.92, 530.81, and 529.55 eV, and they correspond to surface-adsorbed moisture, oxygen defect sites, and lattice oxygen, respectively.[30,31]

The surface morphology of bare twisted carbon yarns is displayed in Figure 3a, with bunches of carbon fibers having 1 mg/cm density (mass/length). In WSCs, the commercial conductive carbon yarn can serve as both a current collector and a substrate for holding active materials. Figure 3b–d illustrates the FESEM images of the twisted MMO-NFs/MWCNT-coated carbon yarn. Here, it can be seen that in Figure 3b–d, the MMO-NFs/MWCNT are densely coated on the carbon yarn. The high-magnification FESEM image in the inset of Figure 3d confirms the presence of MMO-NFs with a network of MWCNT on the surface of the electrode. Here, MWCNTs inside the MMO-NFs can enhance conductivity by facilitating the transportation of electrons due to their conductive nature.[32] An elemental mapping of the MMO-NF/MWCNT coated electrode through EDX can be seen in Figure 3e, in which elements such as Mg, M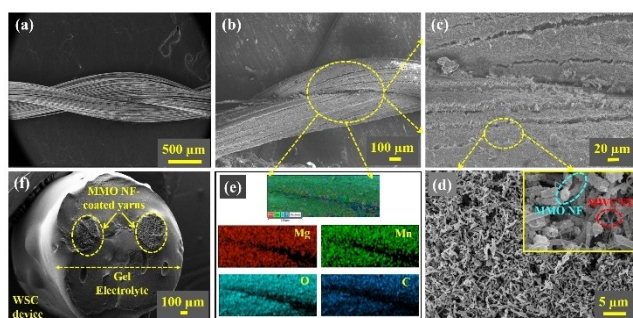n, O, and C are uniformly distributed across the electrode surface. Densely coated MMO-NFs/MWCNTs may enhance the electrochemical properties of WSC devices with their tuned nanostructured geometry. The cross-section of the fabricated WSC device is shown in Figure 3f. The gel layer in between two MMO-NFs/MWCNT coated carbon yarn electrodes fulfils a dual role, serving as both an electrolyte and a separator.

All flexible WSC devices are electrochemically characterized in two electrode configurations. Figure 4a displays the cyclic voltammetry (CV) plots for all the WSC devices using a scan rate of 10 mV/s. Within the 0–1.5 V voltage window, all the CV curves are quasi-rectangular, indicating the mechanism of pseudocapacitive charge storage.[33] The maximum area under the CV curve for the MC-WSC device shows enhanced pseudocapacitive charge storage compared to the M-WSC and C-WSC devices. Figure 4b illustrates the galvanostatic charge-discharge (GCD) curves for all WSC devices, conducted at 0.1 mA/cm current rate. In all cases, the charge-discharge curves exhibit a triangular shape, complementary to CV curves and suggesting a pseudocapacitive charge storage mechanism that involves electron transfer both on the surface and in the bulk of active materials as a result of redox reactions. The maximum discharge time of the MC-WSC device indicates its enhanced electrochemical performance compared to the M-WSC and C-WSC devices. This MC-WSC device features an almost symmetric
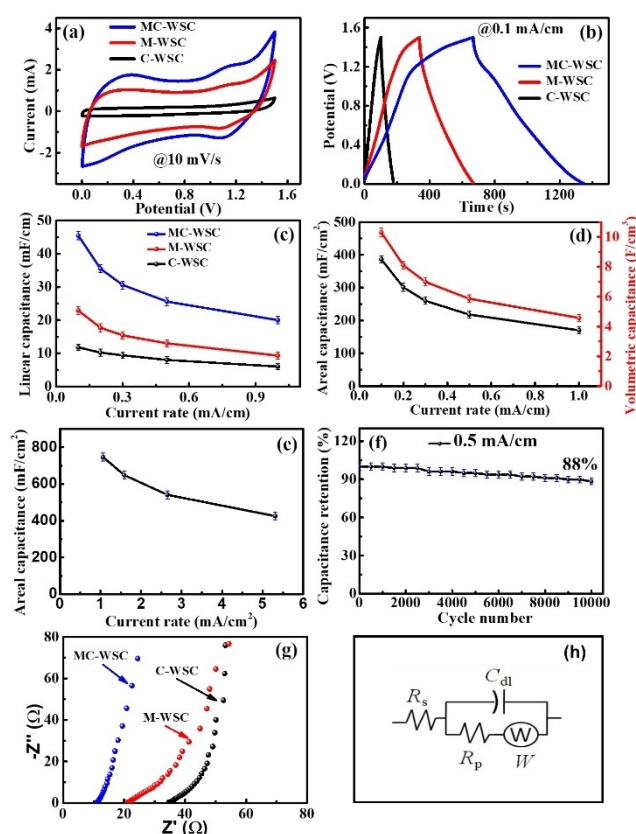
Figure 4. Electrochemical properties of MC-WSC, M-WSC, and C-WSC devices: (a) CV graphs @10 mV/s scan rate, (b) GCD graphs @0.1 mA/cm current rate, (c) linear capacitance vs. current rate, (d) areal capacitance and volumetric capacitance vs. current rate plot of MC-WSC, (e) areal capacitance vs. areal current rate plot of MC-WSC, (f) cyclability plot of MC-WSC, (g) EIS plots, and (h) equivalent electrical circuit.

Figure 3. FESEM images of (a) bare carbon yarn, (b–d) MMO-NF-coated carbon yarn, (e) EDX elemental mapping of MMO-NF-coated carbon yarn, (f) cross-section FESEM of WSC device.

Batteries & Supercaps

Research Article
doi.org/10.1002/batt.202400176

**Chemistry
Europe**

European Chemical
Societies Publishing

Table 2. Comparing the performance of various flexible WSC devices.

Active material	Substrate	Preparation method	Capacitance	Capacitance retention	Ref.
$NiCo_2O_4$/rGO	Ni wire	Hydrothermal/ Solvothermal	342 mF/cm³, 3.11 mF/cm², and 0.39 mF/cm at 200 μA	–	[12]
$NiFe_2O_4$	Carbon yarn	Dip coating	247 μF cm⁻¹ at 10 mV/s	96% after 8000 cycles	[23]
$MnCo_2O_4$	Cu wire	Electrodeposition	20.6 mF cm⁻¹ and 54.8 mF cm⁻² at 65 μA cm⁻¹	93.7% after 5000 cycles	[36]
$NiCo_2O_4$/MnO_2	Ni wire	Hydrothermal	105.4 mF cm⁻² at 200 μA	84% after 3000 cycles	[37]
Mn_3O_4/MWCNT	Ni wire	Hydrothermal/Dip coating	2.22 mF/cm² and 0.40 mF/cm at 25 μA	83% after 3000 cycles	[38]
MnO_2 and MoO_3	Carbon fiber	Electrodeposition	4.86 mF cm⁻² at 0.5 mA cm⁻²	89% after 3000 cycles	[39]
$MgMn_2O_4$/MWCNT	Carbon yarn	EPD	45.5 mF cm⁻¹, 386 mF cm⁻² and 10.3 F cm⁻³ at 0.1 mA/cm 440 mF cm⁻² at 10 mV/s	88% after 10,000 cycles	This work

charge/discharge curve, indicating a high coulombic efficiency (99.5%) and reversible redox process. For all WSC devices, the linear capacitances at various current rates within the range of 0.1–1 mA/cm are analyzed utilizing equation 1, as depicted in Figure 4c. At a current rate of 0.1 mA/cm, the flexible MC-WSC device achieved the highest linear capacitance of 45.5 mF/cm, which is superior as compared to C-WSC (11.8 mF/cm at 0.1 mA/cm) and M-WSC (22.9 mF/cm at 0.1 mA/cm) devices.

A plot of the areal and volumetric capacitance values for the MC-WSC device is shown in Figure 4d, where the values were calculated at various current rates using equations 2&3, respectively. At 0.1 mA/cm, the MC-WSC device exhibits an areal capacitance of 386 mF/cm² and a volumetric capacitance of 10.3 F/cm³. Further, the values of areal capacitances have also been calculated by applying an areal current rate and plotted in Figure 4e. The WSC shows an areal capacitance of 747 mF/cm² at 1 mA/cm². The values of capacitances are reduced at higher current rates, as depicted in Figure 4c-e, which is associated with the fact that at higher current rates, surface-controlled charge storage dominates over diffusion-controlled intercalation. As the current rate increases, electrolytic ions do not have enough time to diffuse and fully utilize all available active sites within a material matrix, leading to a reduction in capacitance.[34]

Figure 4f presents the cycle life of the MC-WSC device, illustrating its behaviour over 10,000 cycles at 0.5 mA/cm² through the GCD technique. The device indicates good stability by displaying capacitance retention of 88% ($\pm$2%) after 10,000 cycles. Compared with various wire/fiber/yarn-shaped SC devices fabricated utilizing various spinel metal-oxides and Mn-oxide active materials in the literature, the MC-WSC device shows superior electrochemical performance, as tabulated in Table 2. For the MC-WSC device, the high electrochemical performance is ascribed to the unique and dense hierarchically distributed network of electroactive materials (MMO-NFs and MWCNT) on the conductive carbon yarn surface. It is worthwhile noting that despite the absence of inactive polymer binders, the enhanced ionic conduction and charge transport are favoured by the hierarchically designed binder-free architecture of the active materials.[35] Here, MMO-NFs enhanced the electrochemical capacitance by enabling the pseudocapacitive

redox reactions, and MWCNT facilitates the transfer of charge by serving as electronic conducting wiring between the MMO-NFs and conductive carbon yarn substrate. Hence, the modified EPD-grown architecture of the MMO-NFs and MWCNT on conductive carbon yarn: (i) avoids the use of insulative polymer binders that act as dead weight, (ii) promotes ionic conduction by the penetration of electrolytic ions and reduces their diffusion length in the modified structure, (iii) increases the electrode/electrolyte contact area, (iv) minimizes the contact resistance between active materials and current collector, (v) improves the electrochemical performance of WSC device leading by the effective utilization of more electrochemically active sites.

The EIS analysis for all the WSC devices is performed, as shown in Figure 4g. The experimentally measured EIS plots are fitted using ZView software utilizing an electrical equivalent circuit,[40] as illustrated in Figure 4h. In the equivalent circuit, the ohmic resistance is represented by R_s.[41] The R_p represents the faradic charge transfer resistance at the electrode/electrolyte interface, whereas C_{dl} represents the capacitance associated with the double layer.[42] Warburg impedance (W) measures the resistance during the process of ion transportation and diffusion within the active materials.[43] All the parameters are obtained by fitting the EIS plots, as displayed in Table 3. Within SC systems, the equivalent series resistance (ESR) is the result of the combined contributions of R_s and R_p. The values of ESRs for MC-WSC, M-WSC and C-WSC devices are 11.4, 21.8, and 35.1 Ω, respectively. The lower value of ESR for the MC-WSC device is ascribed to the synergic effect of MMO-NFs with voids/pores and MWCNTs, which exhibit smaller ohmic and charge-transfer resistance due to more electrode/electrolyte contact area through the penetration of electrolytic ions into their interior

Table 3. Electrical fitted parameters of WSCs.

Parameter	MC-WSC	M-WSC	C-WSC
R_s (Ω/cm²)	10.1	19.6	32.4
R_p (Ω/cm²)	1.3	2.2	2.7
C_{dl} (F/cm²)	2.1×10^{-4}	3×10^{-4}	1.5×10^{-4}
W (Ω/cm²)	23.09	28.31	16.52

Batteries & Supercaps

Research Article
doi.org/10.1002/batt.202400176

Chemistry Europe
European Chemical
Societies Publishing

region. It is worthwhile noting that the lower value of ESR leads to higher power density in a supercapacitive system.[44–46]

For the detailed electrochemical analysis of the MC-WSC device, the CV curves were evaluated at various scan rates between 10 and 100 mV/s, as depicted in Figure 5a. At all scan rates, CV curves display a quasi-rectangular pattern, indicating the mechanism of pseudocapacitive charge storage. Further, the Dunn method[46] is used to calculate the contributions of the current resulting from diffusion-controlled redox reactions and surface reactions to the overall current. The nearly linear current i versus $v^{1/2}$ plot shown in Figure 5b validates the presence of surface redox reactions, confirming the pseudocapacitive charge storage mechanism attributed to MMO NFs in MC-WSC.[47,48] The y-axis intercept on the i versus $v^{1/2}$ plot also signifies the current contribution arising from double-layer formation at the electrode/electrolyte interface, which is attributed to the presence of MWCNT in the MC-WSC device.[49]
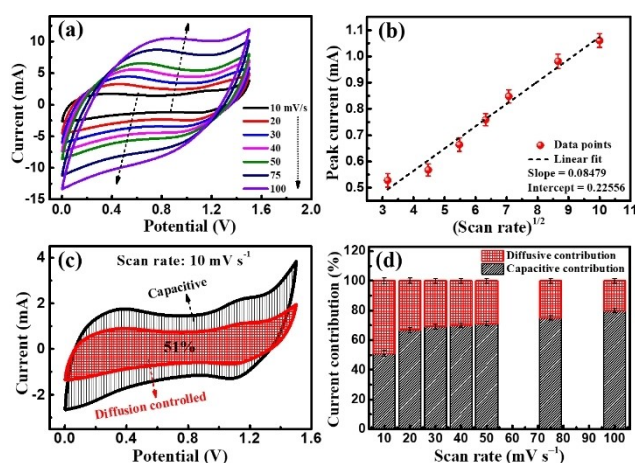
Furthermore, the quantitative contributions of the diffusion and capacitive current to the overall current have been determined at the scan rate of 10 mV/s and plotted in Figure 5c, where the red-shaded region presents the diffusion current and the black-shaded region presents the capacitive current. Figure 5d depicts the percentage of capacitive and diffusion contributions at different scan rates ranging from 10 to 100 mV/s. A noteworthy observation is that the capacitive contribution to the total current exhibits a consistent rise with increasing scan rates. This suggests that the charge storage process is predominantly surface-controlled at higher scan rate values, leading to exceptional cyclic stability and favourable rate capability for the MC-WSC device.[46,50]

Energy and power densities are the most essential matrices used to identify the performance of an SC device.[51] For the MC-WSC device, the values of the linear energy density, linear power density, and areal energy density are evaluated utilizing equations 5, 6, and 7, respectively, as presented in the Ragone plot in Figure 6a. The single MC-WSC device provides a linear energy density of 6.2–14.2 µWh/cm, linear power density of 75–744 µW/cm, and areal energy density of 53–120 mWh/cm². It can be observed that the power and energy density values for MC-WSC devices are better than those of various similar devices based on different materials published in the literature.[12,29,30,52–54] The WSC device should be flexible and mechanically stable in order to serve as a power source for textile-based wearable electronic systems. Thus, the fabricated MC-WSC devices are electrochemically characterized in various bending positions in order to analyze their practicability for energy storage in flexible electronic applications. The MC-WSC device with different bending angles, i.e., 0°, 90°, and 145° is illustrated in Figure 6b. For WSC device, the CV curves are measured at the scan rate of 50 mV/s under various bending positions, as presented in Figure 6c. During different bending positions, the MC-WSC device retains an almost identical pattern of the CV curves, thereby retaining its capacitive performance.[55]
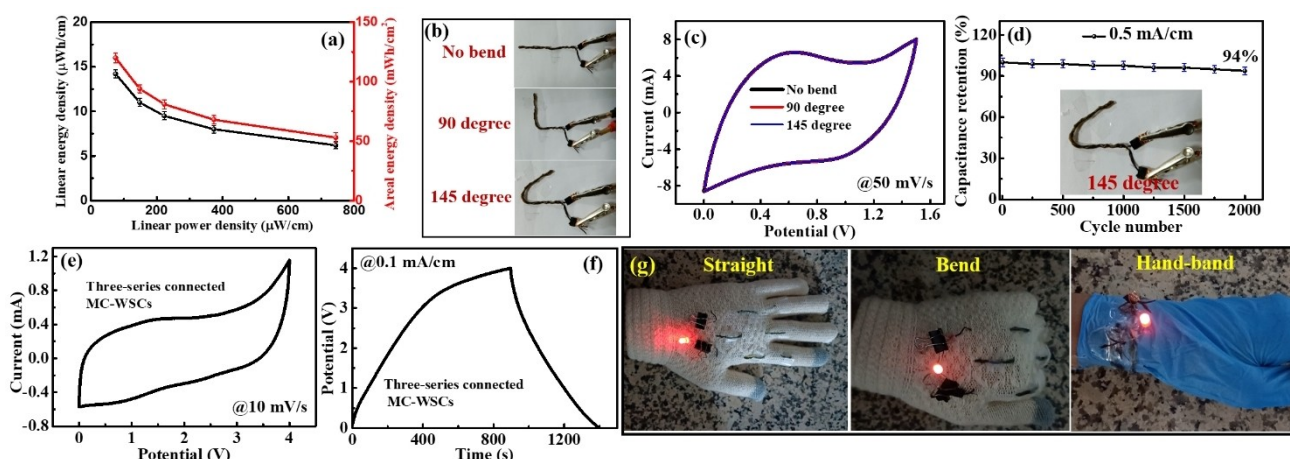

Figure 5. (a) CV graphs @10-100 mV/s scan rates, (b) current i versus v1/2 plot, (c) capacitive and diffusion current at 10 mV s^{-1} scan rate, (d) bar chart with diffusion and capacitive current contributions (in %) at different scan rates.

Figure 6. (a) Ragone plot for MC-WSC device. (b) flexible MC-WSC device in different bending states, (c) CV graphs of the MC-WSC device at different bending states, (d) cyclability plot of MC-WSC device under a bending angle of 145 degrees at a current density of 0.5 mA/cm upto 2000 GCD cycles, (e) CV graphs for three series-connected MC-WSC devices at 10 mV/s, (f) GCD plot of three series-connected MC-WSC devices at 0.1 mA/cm, (g) knitting of three series-connected MC-WSC devices into a wearable hand glove and glowing a red LED in various positions, including straight, bend, and hand-band positions.

Additionally, the charge/discharge performance of the MC-WSC device is investigated for 2000 cycles at a bending angle of 145°, utilizing 0.5 mA/cm current rate (Figure 6d). As the device bends, the resistance and stress on the surface of the device increase slightly, causing a lesser reduction in capacitance.[56,57] As a result of the compact deposition and hierarchically distributed network of MMO-NFs and MWCNTs on the surface of the carbon yarn current collector, the MC-WSC device is flexible and mechanically stable during bending, which may help maintain the MC-WSC device's structural as well as electrical integrity for flexible electronic applications. Additionally, the MC-WSC device has high durability because the carbon yarn substrate has excellent flexibility and mechanical strength, while the gel electrolyte provides excellent flexibility during extreme bending conditions and holds the device's components together.[58,59]

We also investigated MC-WSC device as a power source for realistic and practical textile applications. Three identical MC-WSC devices are woven into a wearable hand glove, which is connected in a series connection. For the assembled devices, the GCD and CV data plots are evaluated at a current rate of 0.1 mA/cm and a scan rate of 10 mV/s, respectively, in 0 to 4 V voltage window, as depicted in Figure 6e and f. The series-connected three WSCs light up a red LED in the straight, bend and hand-band positions, as shown in Figure 6g. Moreover, the devices illuminate a red LED for more than 5 minutes at different bending angles, which is also demonstrated in the video. Therefore, the reported flexible WSC device in this manuscript can provide adequate power and energy density, including excellent flexibility, wearability, and stability under various bending conditions, which fulfils the requirement of low-power flexible electronic applications. These outcomes are attractive for a flexible and wearable multifunctional electronic systems. Hence, the above study demonstrates that the fabricated WSC device can be utilized to power next-generation smart textiles for application in wearable electronics.

3. Conclusions

This article presented the fabrication of a flexible WSC device by depositing 1D and porous MMO-NFs and MWCNT over highly flexible and conductive carbon yarn substrate through the binder-free in situ co-electrophoretic deposition technology for application in flexible wearable electronics. The modified architecture of the fabricated electrodes facilitates the ionic/electronic conduction in the WSC device due to the hierarchically designed network of active materials. The developed flexible WSC device is capable of delivering capacitances of 386 mF/cm^2 and 45.5 mF/cm at a current density of 0.1 mA/cm. Additionally, at 0.5 mA/cm current density, the WSC device retains 88% of its initial capacitance after 10,000 cycles and 94% of its initial capacitance following 2000 bending cycles, confirming its good mechanical and electrochemical properties. Further, the MC-WSC device delivered an energy density of 14.2 μWh/cm and a power density of 744 μW/cm. Furthermore, a red LED is lit using a series connection of WSC devices knitted

in a wearable glove during straight and bending positions, which proves its practical capability as a flexible energy storage device. Therefore, this study presents simple, innovative, and cost-effective strategies for fabricating binder-free flexible supercapacitors with high power and energy density for wearable electronic applications.

Conflict of Interests

The authors declare no competing interests.

Data Availability Statement

The data that support the findings of this study are available from the corresponding author upon reasonable request.

[1] N. He, J. Liao, F. Zhao, W. Gao, *ACS Appl. Mater. Interfaces* **2020**, *12*, 15211–15219.
[2] J. Chen, T. He, Z. Du, C. Lee, *Nano Energy.* **2023**, *117*, 108898.
[3] R. Xu, M. She, J. Liu, S. Zhao, J. Zhao, X. Zhang, L. Qu, M. Tian, *ACS Nano.* **2023**, *17*, 8293–8302.
[4] M. Li, Z. Li, X. Ye, W. He, L. Qu, M. Tian, *Adv. Funct. Mater.* **2023**, *33*, 2210111.
[5] I. Marriam, M. Tebyetekerwa, Z. Xu, H. Chathuranga, S. Chen, H. Chen, J. C. Zheng, A. Du, C. Yan, *Energy Storage Mater.* **2021**, *43*, 62–84.
[6] M. Li, Z. Li, X. Ye, X. Zhang, L. Qu, M. Tian, *ACS Appl. Mater. Interfaces.* **2021**, *13*, 17110–17117.
[7] X. Qian, R. Qiu, C. Lu, Y. Qiu, Z. Wu, S. Wang, K. Zhang, *ACS Omega.* **2020**, *5*, 4697–4704.
[8] B. Pandit, C. D. Jadhav, P. G. Chavan, H. S. Tarkas, J. V. Sali, R. B. Gupta, B. R. Sankapal, *IEEE Trans. Power Electron.* **2020**, *35*, 11344–11351.
[9] D. B. Murray, J. G. Hayes, *IEEE Trans. Power Electron.* **2015**, *30*, 2505–2516.
[10] Z. Li, Y. Ma, L. Wang, X. Du, S. Zhu, X. Zhang, L. Qu, M. Tian, *ACS Appl. Mater. Interfaces.* **2019**, *11*, 46278–46285.
[11] Y. Wua, Q. Wanga, T. Lia, D. Zhanga, M. Miao, *Electrochim. Acta* **2017**, *245*, 69–78.
[12] P. S. Shewale, K. S. Yun, *Nanomaterials* **2021**, *11*, 852.
[13] S. Rani, Y. Sharma, *IEEE Trans. on Power Electron.* **2022**, *37*, 13022–13029.
[14] J. H. Kim, C. Choi, J. M. Lee, M. J. de Andrade, R. H. Baughman, S. J. Kim, *Sci. Rep.* **2018**, *8*, 13309.
[15] A. S. Binfaris, A. G. Zestos, J. L. Abot, *Energies* **2023**, *16*, 5736.
[16] N. Lima, A. C. Baptista, B. M. M. Faustino, S. Taborda, A. Marques, I. Ferreira, *Sci. Rep.* **2020**, *10*, 7703.
[17] C. Yang, Q. Liu, L. Zang, J. Qiu, X. Wang, C. Wei, X. Qiao, L. Hu, J. Yang, G. Song, C. Liu, *Adv. Electron. Mater.* **2019**, *5*, 1.
[18] A. Tandon, S. Rani, Y. Sharma, *ACS Appl. Energ. Mater.* **2022**, *5*, 6855–6868.
[19] Q. Zhou, C. Jia, X. Ye, Z. Tang, Z. Wan, *J. Power Sources.* **2016**, *327*, 365–373.
[20] S. Rani, Y. Sharma, *IEEE Trans. on Power Electron.* **2022**, *37*, 13022–13029.
[21] P. Zhao, X. Ye, Y. Zhu, H. Jiang, L. Wang, Z. Yue, Z. Wan, C. Jia, *Electrochim. Acta.* **2018**, *281*, 717–724.

Batteries & Supercaps

Research Article
doi.org/10.1002/batt.202400176

Chemistry
Europe
European Chemical
Societies Publishing

[22] S. Rani, N. Kumar, Y. Sharma, *Adv. Electron. Mater.* **2022**, *8*, 2200108.

[23] P. Zhao, X. Ye, Y. Zhu, H. Jiang, J. Pan, Z. Wan, C. Jia, C. Yang, *J. Power Sources* **2019**, *442*, 227188.

[24] C. Choi, H. J. Sim, G. M. Spinks, X. Lepró, R. H. Baughman, S. J. Kim, *Adv. Energy Mater.* **2016**, *6*, 1502119.

[25] C. S. Yeo, Y. J. Heo, M. K. Shin, J. H. Lee, Y. Y. Park, S. J. Mun, Y. A. Ismail, L. H. Sinh, S. J. Park, S. Y. Park, *ACS Appl. Energ. Mater.* **2021**, *4*, 8059–8069.

[26] A. Tandon, Y. Sharma, *ACS Appl. Mater. Interfaces* **2024**, Article ASAP.

[27] T. Dong, P. Mu, S. Zhang, H. Zhang, W. Liu, G. Cui, *Electrochem. Energy Rev.* **2021**, *4*, 545–565.

[28] J. Yang, M. Xu, J. Wang, S. Jin, B. Tan, *Sci. Rep.* **2018**, *8*, 4200.

[29] M. Zheng, H. Tang, L. Li, Q. Hu, L. Zhang, H. Xue, H. Pang, *Adv. Sci.* **2018**, *5*, 1700592.

[30] C. Si, J. Zhang, Y. Wang, W. Ma, H. Gao, L. Lv, Z. Zhang, *ACS Appl. Mater. Interfaces* **2017**, *9*, 2485–2494.

[31] A. Tandon, Y. Sharma, *J. Alloys Compd.* **2023**, *952*, 169913.

[32] H. Fang, S. Zhang, W. Liu, Z. Du, X. Wu, Y. Xing, *Electrochim. Acta.* **2013**, *108*, 651–659.

[33] N. K. Mishra, R. Mondal, T. Maiyalagan, P. Singh, *ACS Omega* **2022**, *7*, 1975–1987.

[34] M. K. Sahoo, G. R. Rao, *Nanoscale Adv.* **2021**, *3*, 5417–5429.

[35] Z. Chen, L. Zheng, T. Zhu, Z. Ma, Y. Yang, C. Wei, L. Liu, X. Gong, *Adv. Electron. Mater.* **2019**, *5*, 1.

[36] Y. Jia, J. Xie, J. Wu, Y. Yang, X. Z. Fu, R. Sun, C. P. Wong, *J. Power Sources* **2018**, *393*, 54–61.

[37] J. Zhang, P. S. Shewale, K. S. Yun, *Energies* **2019**, *12*, 3127.

[38] P. S. Shewale, K. S. Yun, *J. Alloys Compd.* **2022**, *911*, 164939.

[39] J. Noh, C. M. Yoon, Y. K. Kim, J. Jang, *Carbon* **2017**, *116*, 470–478.

[40] K. P. Gautam, D. Acharya, I. Bhatta, V. Subedi, M. Das, S. Neupane, J. Kunwar, K. Chhetri, A. P. Yadav, *Inorganics* **2022**, *10*, 86.

[41] N. O. Laschuk, E. B. Easton, O. V. Zenkina, *RSC Adv.* **2021**, *11*, 27925.

[42] A. E. Elkholy, A. S. Dhmees, F. E. T. Heakal, M. A. Deyab, *New J. Chem.* **2019**, *43*, 1987–1992.

[43] E. S. Agudosi, E. C. Abdullah, A. Numan, N. M. Mubarak, S. R. Aid, R. B. Vilau, P. G. Romero, M. Khalid, N. Omar, *Sci. Rep.* **2020**, *10*, 11214.

[44] C. Portet, P. L. Taberna, P. Simon, E. Flahaut, C. Laberty-Robert, *Electrochim. Acta* **2005**, *50*, 4174–4181.

[45] J. C. Gutiérrez, A. Celzard, V. Fierro, *Front. Mater.* **2020**, *7*, 217.

[46] V. Augustyn, J. Come, M. A. Lowe, J. W. Kim, P. L. Taberna, S. H. Tolbert, H. D. Abruña, P. Simon, B. Dunn, *Nat. Mater.* **2013**, *12*, 518–522.

[47] L. Yu, G. Z. Chen, *Front. Chem.* **2019**, *7*, 272.

[48] S. Liu, L. Kang, J. Hu, E. Jung, J. Zhang, S. C. Jun, Y. Yamauchi, *ACS Energy Lett.* **2021**, *6*, 3011–3019.

[49] N. M. Shinde, P. V. Shinde, J. M. Yun, K. C. Gunturu, R. S. Mane, C. O'Dwyer, K. H. Kim, *ACS Omega* **2020**, *5*, 9768–9774.

[50] Y. K. Wang, M. C. Liu, J. Cao, H. J. Zhang, L. B. Kong, D. P. Trudgeon, X. Li, F. C. Walsh, *ACS Appl. Mater. Interfaces* **2020**, *12*, 3709–3718.

[51] R. Barik, V. Tanwar, R. Kumara, P. P. Ingole, *J. Mater. Chem. A* **2020**, *8*, 15110–15121.

[52] Y. F. Wang, H. T. Wang, S. Y. Yang, Y. Yue, S. Wie Bian, *ACS Appl. Mater. Interfaces* **2019**, *11*, 30384–30390.

[53] Q. Wang, D. Zhang, Y. Wu, T. Li, A. Zhang, M. Miao, *Energy Technol.* **2017**, *5*, 1–9.

[54] X. Liang, Q. Wang, Y. Ma, D. Zhang, *Dalton Trans.* **2018**, *47*, 17146.

[55] Y. Song, X. X. Chen, J. X. Zhang, X. L. Cheng, H. X. Zhang, *IEEE J. Microelectromechanical Systems* **2017**, *26*, 1055–1062.

[56] H. T. Jeong, J. F. Du, Y. R. Kim, *ChemistrySelect* **2017**, *2*, 6057–6061.

[57] R. Tjandra, W. Liu, M. Zhang, A. Yu, *J. Power Sources* **2019**, *438*, 227009.

[58] Y. N. Liu, J. N. Zhang, H. T. Wang, X. H. Kang, S. W. Bian, *Mater. Chem. Front.* **2019**, *3*, 25.

[59] Y. Zhu, H. Jiang, X. Ye, Z. Yue, L. Wang, C. Jia, *J. Power Sources* **2020**, *460*, 228108.